

Explosion Temperature and Dispersion Characteristics of Composite Charges Based on Different Non-detonative Materials

Xiao-wen Hong,^[a] Wei-bing Li,^{*[a]} Xiao-ming Wang,^[a] Wen-bin Li,^[a] and Rui Li^[a]

Abstract: The explosion fireball temperature and scattering process of explosive products of annular composite charges were investigated to guide the selection of non-detonative materials with controllable composite charge output. Overpressure sensors, an infrared thermal imager, and a high-velocity photography system were used to compare the explosive fireball temperature, scattering movement, and post-combustion characteristics of composite charges with different non-detonative materials. The fireball temperature distributions of the active non-detonative materials (rubber containing various proportions of aluminum powder) were not uniform, and the heat radiation power, heat flux, and overpressure were relatively high and first decreased and then increased with increasing aluminum powder content.

The active non-detonative materials had two high-temperature regions in the lateral direction. Oxygen-free explosions, anaerobic combustion, and post-combustion processes occurred during the energy-release reaction of the composite charges. The temporal evolution of the throwing radius of the explosion products of the composite charges was investigated, and the rate of scattering of the non-detonative materials was analyzed. The rate of scattering was higher than that of an inert non-detonative material (polyurethane) and first increased and then decreased with increasing aluminum powder content. Based on the explosion-proof performance and heat radiation energy output characteristics, rubber containing 50% aluminum was selected as the optimal non-detonative material.

Keywords: Composite charge · Non-detonative material · Explosive fireball temperature · Dispersion radius

1 Introduction

The modern battlefield environment is becoming increasingly complex. For tasks with very strict rules of engagement, such as combating targets in urban areas or providing fire support to areas close to friendly forces, conventional ammunition has high damage power and can easily inflict collateral damage, making its use unsuitable. Therefore, a new ammunition system concept is needed that allows different energy outputs to be selected for different target types to achieve accurate damage to the target. With the strong demand for modern warfare, research on the controllable output of warhead power has received extensive research attention [1–4]. In 2012, QinetiQ proposed a multi-layer annular nested composite charge structure, which consists mainly of an aluminum-containing explosive layer, a middle explosive layer, and an internal high-detonation layer. The center charges detonate for partial detonation of a warhead, whereas the internal and external charges simultaneously detonate for full detonation [5]. Haskins [6] proposed a similar charge structure for a warhead; he described the composition of the composite charge structure, material formulation, and detonation assembly and verified the feasibility of the energy output of the charge structure. The above studies mainly focused on the composite charge structure of fixed components and

compared the differences in the energy output of the warheads under different modes, with less focus on the effect of changes in the material used for the mid-level blasting layers on the energy output of warheads.

Research on composite charges is concentrated on dual composite charges or thermobaric charges with highly explosive internal cores. Trzciński et al. [7] used shock wave overpressure sensors and photodiodes to study the explosion characteristics of multi-layered warm-pressure explosives in closed, incompletely sealed explosion chambers, and the extent of reaction of the outer explosive was determined using thermogravimetric/differential thermal analysis (TG/DTA) and X-ray diffraction (XRD) analysis of the explosive products. In addition, these researchers used X-ray photography to track the curvature of the outer charge shock wave and showed that the detonation phenomenon does not occur in the outer charge [8]. Paszula et al. [9] studied the explosion parameters of explosive mixtures of ammonium nitrate (AN) and aluminum powder (Al) composite phases and tested the shock wave overpressure and

[a] X.-w. Hong, W.-b. Li, X.-m. Wang, W.-b. Li, R. Li
ZNDY of Ministerial Key Laboratory, Nanjing University of Science and Technology, Nanjing, P. R. China
Tel: +86 84315059
*e-mail: njjustlw@163.com

specific impulse. The results indicated that the peak overpressure of the shock wave of AN/Al explosives was lower than that for the same mass of thermobaric charges with internal RDXph core. Zheng et al. [10] monitored the scattering process of the explosive product of a composite thermobaric charge using a high-velocity motion analysis system and investigated the temporal evolution of the dispersion radius of the explosive product. Currently, research on the structural form of a controlled multi-layer charge remains in the exploration stage, with few reports available in the literature. Achieving controllable output of warhead power requires that the damage be characterized by both point and surface killing. The explosion of composite-charge explosives in central detonation mode differs from that of thermobaric charges, and the damage should be characterized by point killing to reduce collateral damage. Therefore, analyzing the explosion temperature of fireballs and scattering process of explosive products with the detonating mode of the center, determining the dispersion radius, and optimizing non-detonative materials have important theoretical guidance and engineering application value for achieving controllable output energy of warheads.

In this study, overpressure testing and infrared thermal imaging temperature measurement of an annular composite charge structure in central detonation mode were conducted. High-velocity photography was used to monitor the inert material, explosion of the fireball under the active material, and cloud scattering process of the explosive product. The temperature characteristics of explosive fireballs of composite charges under two types of non-detonative materials were analyzed, and the temporal evolution of the dispersion radius of scattering of the exploding explosives of the composite charges was investigated.

2 Experimental Design

2.1 Characteristics of Charges

The experimental charge used in this study was a circular composite structure, as shown in Figure 1, with a diameter of 95 mm, including a center JH-2 charge layer, middle non-detonative material layer, and outer blunt aluminiferous explosive ring charge layer. The height of the structure was 80 mm, and the detonation was initiated at the center of the upper end. The explosion characteristics of the explosive fireballs and explosion products of composite charg-

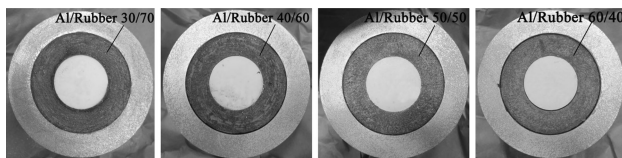


Figure 1. Test charges.

es under different non-detonative materials, polyurethane and rubber containing different volumetric proportions of Al (30%, 40%, 50%, and 60%), were investigated in a comparative study.

The aluminum-containing rubber used in this paper is a non-explosive material. It may be any material that is itself not capable of sustaining detonation; otherwise the high explosive portions and the outer aluminum-containing explosive may all detonate simultaneously (i.e. sympathetic detonation may occur), then the energy output of the composite charge is not adjustable. For the selection of non-detonative materials, it can comprise inert materials such as polymers or rubbers, and it can comprise high energy materials (such as active metal powders), but this material itself does not have an explosive property, forming a new form of inert and high-energy materials through melting and pressing. The composite material can better combine the advantages of inert materials and active materials. Advantageously, the non-detonative material can comprise a high energy material so as to compensate for the reduction in the total volume/mass of high explosive missing [6]. The use of aluminum particles to enhance blast is well known and is a highly preferred additive, then aluminum-containing rubber as a non-detonative material was studied in this paper.

2.2 Experimental Site

Figure 2 presents a schematic illustration of the experimental layout. A grain was placed on a 1-m-high wooden platform. The end face of the pressure sensor was flush with the ground surface and 2-m-away from the grain. Blast wave overpressure data were recorded using a shock wave storage tester. The internal sensor was an 113B21 piezoelectric pressure sensor (United States PCB Company), and the sampling frequency was 1 MSa/s.

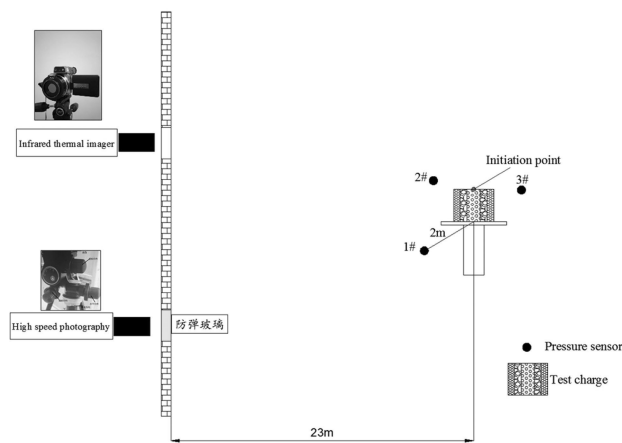


Figure 2. Schematic illustration of experimental layout.

An infrared thermal imager and high-velocity photographic-testing column were located 23 m away from the platform. The infrared thermal imager was used to monitor the temperature characteristics of the explosive fireball. An InfReC R500 series Avio high-resolution system (Europe and Earth Technology Co., Ltd.) was used to record images of the explosion fireball. Parameters of 640 (H) \times 480 (V) detector pixels, a frame frequency of 30 Hz, and a temperature range of -40°C to 2000°C were selected. The emissivity of the infrared thermal imager was set to 0.42 based on previous experimental experience and the emissivity range of the explosion products given in the literature [11].

To compensate for the disadvantages of the low sampling frequency and unclear contours of the infrared thermal imaging system, high-velocity photographic systems were used to record the growth process of the explosive fireballs and scattering process of the explosive products of the different composite charges. A Fastcam nltima APX high-velocity camera (Japan Photron Corporation) was used with a shooting rate of 4000 frames/s and a maximum resolution of each frame of 1280 (H) \times 960 (V).

3 Experiment Results and Analysis

3.1 Overpressure and Temperature Distribution Characteristics of Explosive Field in Composite Charge

The radiation thermometer is used in this paper is different from the spectral temperature measurement in literature [12–13]. The spectrum method sometimes can only get the temperature of some places of the explosion source, the maximum temperature changes with the time in the reaction process and the temperature measurement of the oxygen free combustion stage. The composite charge explosion has a characteristics of cloud explosion. The infrared thermal imaging technology used in this paper can get the time and space distribution of the explosive temperature field of the composite charge. Thus, the infrared thermal imaging technology is more suitable for measuring the large area high temperature in the cloud cluster explosion. The temperature measured by the infrared thermal imager is mostly the phase of the oxygen combustion of the explosive, due to the sampling frequency limitation. The energy output difference of the composite explosive with different non-detonative materials can be compared and the non-detonative material with better performance be found by using the infrared thermal imager. Therefore, it is feasible using the infrared thermal imager to measure the temperature.

3.1.1 The Theory of Measuring Temperature

The thermal radiation of the object is mainly in the infrared band (0.76~1000 m), when the infrared thermography was

used to detect ground targets, the temperature of ground background is usually 300 K and the maximum contrast wavelength is approximately 8 μm . The wavelength interval was taken between 8 and 14 μm as the detection band without other factors. When the infrared thermal imager is used to measure the temperature, the temperature measurement lens receives the radiation ability from the target, and the detector converts it to the voltage signal, that is, the detector responds to the gray value [14]. There is a correlation between pixel response gray value and actual temperature, and the theory of temperature measurement is given in Figure 3.

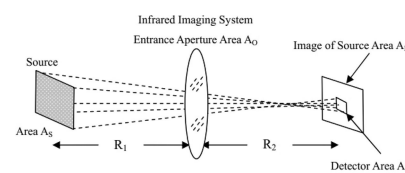


Figure 3. Infrared imaging system directly viewing a source.

The distance between the radiant source and the thermal imager is R_1 , the distance between the lens to the radiation source image plane is R_2 and the detector area is A_d , then the output voltage of the infrared thermal imager system can be expressed as:

$$U_s = G \int_{\lambda_1}^{\lambda_2} R(\lambda) \frac{\pi L_e A_d}{4(f/\#)^2(1+M)^2} \tau_s(\lambda) \tau_a(\lambda) d\lambda \quad (1)$$

Where the system gain is G , the system spectral response is band limited from λ_1 to λ_2 , $R(\lambda)$ is the detector's responsivity, L_e is the spectral radiant responsivity, $(f/\#)$ is the system's optical F-number, $\tau_s(\lambda)$ is the system's optical transmittance, $\tau_a(\lambda)$ is the atmospheric transmittance, and $M=R_1/R_2$ is the magnification. The equations (1) indicates that the output of the infrared thermal imager is related to the characteristics of the radiant source, the characteristics of the thermo imager itself and the atmospheric correlation between the radiant source and the thermal imager. When the emissivity of the target and the distance R_1 are determined, the result of the temperature measurement is only related to the atmospheric characteristics between infrared thermal imager and the target. The accuracy of infrared thermal imager can be improved by calculating $\tau_a(\lambda)$ accurately.

It is obvious that the atmospheric transmittance is not only related to the surroundings temperature, humidity, background temperature and measuring distance, but also to wind speed, air pressure, atmospheric quality and chemical component. At present, correction functions of environmental parameter can be set by most infrared thermal imaging devices, but the calibration process is mostly carried out under standard atmospheric pressure or laboratory

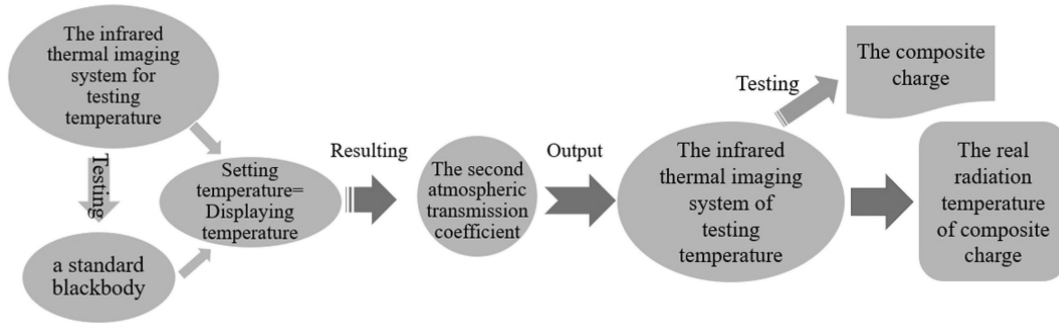


Figure 4. Flow chart of testing temperature in field.

environment. For complex environments such as explosion fields, the software can only partially restore its atmospheric parameters. If the accurate temperature measurement of the target is to be achieved in the explosion field, the atmospheric transmittance must be modified. In this paper, the atmospheric transmittance is corrected by the temperature of a standard blackbody, which can correct the temperature displayed in window by the infrared thermal imaging devices [15].

3.1.2 Calibration Procedures for Infrared Thermometers

The composite charge for non-detonative materials composed of polyurethane was used as the target of radiation to be tested. The measuring theory of the radiant temperature for the composite charge in field is shown as Figure 4.

The Mikron M330 high temperature black body furnace was used as the standard black body. The temperature range is 300~1700 °C, and the effective emissivity is 0.99. The operator only needs to input some parameters of environment which can be used to calculate the atmospheric transmission coefficient with the convergent way or LOWTRAN 7 model in software. Then, the operator focuses the temperature measuring system to finish the measuring process. The M330 blackbody furnace was placed at the blasting position, the blackbody furnace temperature was set at 600 °C, 800 °C, 1000 °C and 1200 °C respectively, and the measured temperature of the infrared thermal imager at the set temperature was also recorded, then the atmospheric transmittance in setup bars is adjusted to make the displayed temperatures in window equal to the set temperature of the blackbody. The atmospheric transmittance in setup bars of system is the numerical value which will be used of the subsequent temperature measurement of the composite charge, here, the displayed temperature in window of the infrared thermal imaging devices is the true temperature of the composite charge. The atmospheric transmittance of the environment calculated by the LOWTRAN 7 software is 0.893, the true temperature of the black body and the corrected atmospheric transmittance measured by the infrared thermal imager are shown in Table 1.

Table 1. Measuring result for the second atmospheric transmission.

Setpoint Temperature [°C]	True Temperature [°C]	Calculative Atmospheric Transmission	Corrected Atmospheric Transmission
600.0	558.4	0.893	0.803
800.0	732.6	0.893	0.781
1000.0	900.1	0.893	0.776
1200.0	1068.3	0.893	0.770
1400	1196.6	0.893	0.751

The 8 observation points were taken from the surface of the fireball temperature, which were measured by the infrared thermal imager within 140 ms and the average value was obtained. According to the result of Table 1, the temperature average value within 140 ms is divided into the corresponding temperature range. The temperature results measured by infrared thermal imaging of the transmittance and the unmodified atmospheric transmittance were fitted by least squares method, and the results are shown in Figure 5.

The temperature obtained by the modified atmospheric transmittance after calibration by the blackbody furnace are

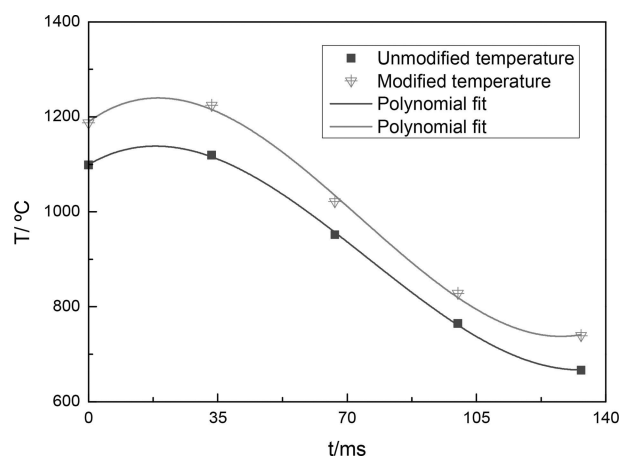


Figure 5. Modified and unmodified average temperature curve of fireball surface.

Table 2. Blast wave overpressure and explosion fireball parameters at maximum temperature.

non-detonative material	ΔP_m	T_{\max} [°]	T_{Avg} [°C]	D [m]	H [m]	Q/W	W_0 [W·m ⁻²]
Polyurethane	0.237	2225.17	1252.60	2.89	3.84	834441.20	103769.44
30 %Al/Rubber	0.284	2956.96	1289.35	2.97	3.69	1716182.61	186239.96
40 %Al/Rubber	0.246	2735.97	1240.96	2.99	3.91	1154167.48	123608.27
50 %Al/Rubber	0.237	2735.65	1332.05	2.97	3.66	1740231.42	179146.74
60 %Al/Rubber	0.26	2822.92	1419.40	3.03	3.58	2360700.88	222049.86

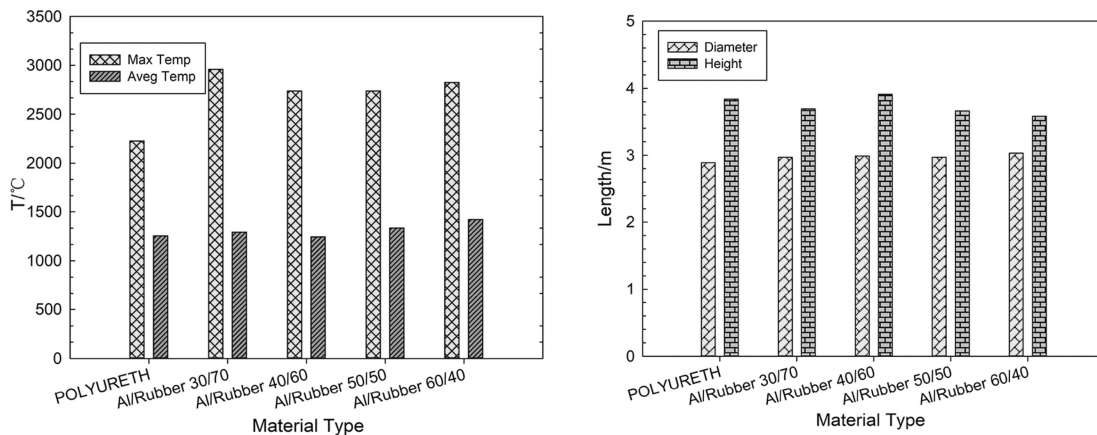


Figure 6. Comparison of a) temperature and b) diameter and height of explosion fireball for different non-detonative materials.

better than the results of the unmodified temperature, which can be seen from Figure 5, and the accuracy of the test is improved to some extent. The subsequent parallel tests are all tested by the calibrated atmospheric transmittance.

3.1.3 Overpressure and Temperature Results

The overpressure and blast fireball of the different non-detonative materials were determined, and the results are presented in Table 2. T_{\max} is the highest temperature on the surface of the explosive fireball, T_{Avg} is the average temperature of the explosive fireball surface when the explosive fireball reached the highest temperature, D is the diameter of the fireball, H is the height of the fireball rise, W_0 is the thermal radiation power per unit area of the fireball, and Q is the heat flux (the total radiated power of the entire fireball surface at a given moment) per unit time.

The principle of the infrared thermal imager is based on Planck's law of blackbody radiation. The measured data W_0 is the radiation intensity of the blackbody, which can be calculated using Boltzmann's law:

$$W_0 = W \cdot T^4 \quad (2)$$

where W is the Boltzmann constant = $5.67 \times 10^{-8} \text{ W}/(\text{m}^2 \text{K}^4)$. However, the general measured object is not an ideal black-

body and can be considered a gray body. The thermal radiation power is related not only to the temperature but also to the surface emissivity. The radiant power of a gray body can be calculated using the following formula:

$$W_0 = X \cdot W \cdot T^4 \quad (3)$$

where T_0 is the reading of the thermal imager; T is the actual temperature of the gray body; and X is the specific emissivity of the gray body surface, which is the emissivity of the infrared thermal imager. After calculating W_0 , Q can be determined by multiplying W_0 by the surface area of the explosive fireball:

$$Q = W_0 \cdot S \quad (4)$$

S can be calculated by processing the infrared thermal image using graphic processing software.

To ensure that the parallel contrast only lists the parameters of the maximum temperature of the explosive fireball surface and sets the lower temperature limit of the infrared thermal imager to 200 °C, the overpressure values in Table 2 were averaged over three sets of test data.

The parameters of the explosion fireball under different non-detonative materials are compared in Figure 6. As observed in Figure 6a, the temperature and average temperature of the explosive fireball for the inert non-detonative material (polyurethane) were low, and the surface temper-

ture of the explosion fireball for the active non-detonative material was higher than that for the inert non-detonative material because of the addition of aluminum powder to the active non-detonative material. As observed in Figure 6b, the radial restraint effect of the non-detonative material led to the explosion of fireballs with smaller heights and larger diameters with increasing aluminum content.

As shown in Figure 6a, the surface temperature of the explosive fireball for the rubber containing 30% aluminum was the highest; however, the maximum temperature of one point in the explosive fireball temperature region does not reflect the overall thermal condition of the fireball. Therefore, the thermal radiation power and heat were calculated from the average temperature of the surface of the fireball. The flux better reflects the heat radiation energy output of the composite charge. Figure 7 presents the normalized heat radiation power, heat flux data, and shock wave overpressure data. The thermal radiation power and heat flux of the aluminum-containing rubber solution were higher than those of the polyurethane solution, indicating that the aluminum powder of the non-detonative materials contributed to the energy release of the post-combustion reaction. With increasing aluminum content, the thermal radiation power and heat flux of each scheme first decreased and then increased, and the law of change was consistent with that of the shock wave overpressure. Improved explosion-proof performance of the non-detonative material led to the reaction of the outer charge being more incomplete and, therefore, lower thermal radiation power and heat flux.

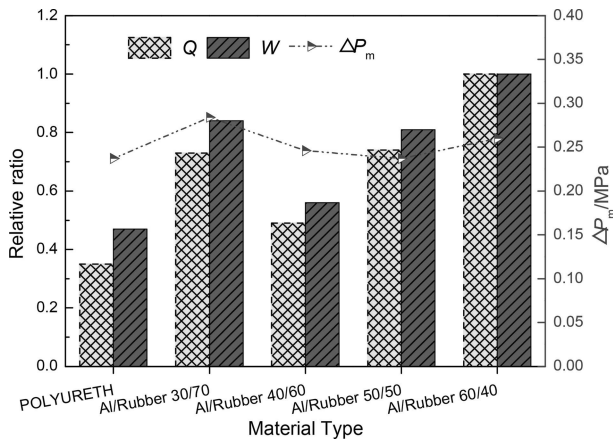


Figure 7. Heat flux, radiant power ratio, and overpressure for explosive fireball of different non-detonative materials.

Figure 7 presents the thermal radiation data. The thermal radiation power and heat flux of polyurethane were the smallest, and those for the non-detonative material containing 60% aluminum were the largest. The values for the materials containing 30% and 50% aluminum were also relatively high, with those for the material containing 40%

aluminum being smaller. The blast wave overpressure data indicate that with increasing aluminum content, the overpressure of the blast wave first decreased and then increased. The blast wave overpressure for aluminum powder ratios of 30% and 50% were 15.4% and 19.8%, respectively, and the change trend of the overpressure data of the blast wave was consistent with those for the thermal radiation power and heat flux.

Scanning electron microscopy (SEM) images of the rubber materials containing different proportions of aluminum powder were obtained in the early stage, as shown in Figure 8. When aluminum powder was added to the rubber as a reinforcing agent, the aluminum powder particles evenly filled the rubber. Natural rubber does not have an obvious network structure; however, when the aluminum powder was added to the rubber, the powder began to accumulate in the rubber in the form of a network structure, as observed in Figure 8, and had a buffering effect on the shock wave. With increasing aluminum content, this buffering effect became more significant and the overpressure measured by the sensor gradually decreased. However, after the aluminum powder content reached a certain level, the spherical aluminum particles began to contact each other and became crowded, making the gap between them very small. The aluminum particles thus became tightly stacked into a multi-level three-dimensional network structure, with the extruded spherical particles “floating” on the material surface, as shown in Figure 8b. The high elasticity of the rubber was gradually reduced, and the material became easy to break, with a reduction of its shear strength and shock wave attenuation effect and increase of the measured shock wave overpressure. Considering the energy loss of the non-detonative material occupying the explosive space and the need to reach the energy output of the warhead, the non-detonative material in the compound charge must not only effectively attenuate the shock wave but also release sufficient energy; therefore, the non-detonative material of rubber containing 50% aluminum is considered optimal for this application.

Infrared images of the explosive fireball of the composite charge for non-detonative materials composed of polyurethane and rubber containing 50% aluminum powder are compared in Figure 9. The distributions of the explosive fireballs of the inert non-detonative materials and active non-detonative materials can be clearly distinguished. When polyurethane was used as the non-detonative material (Figure 9a), the surface temperature distribution of the fireball was more symmetrical and the temperature distribution on both sides was more consistent. When the non-detonative material was rubber containing 50% aluminum (Figure 9b), the explosive fireball distribution was clearly asymmetric, with the temperature on the right side being higher than that on the left. The reason for this difference is that the natural rubber matrix and aluminum powder were evenly mixed; however, during the static detonation process, the tensile strength of the molecular chain

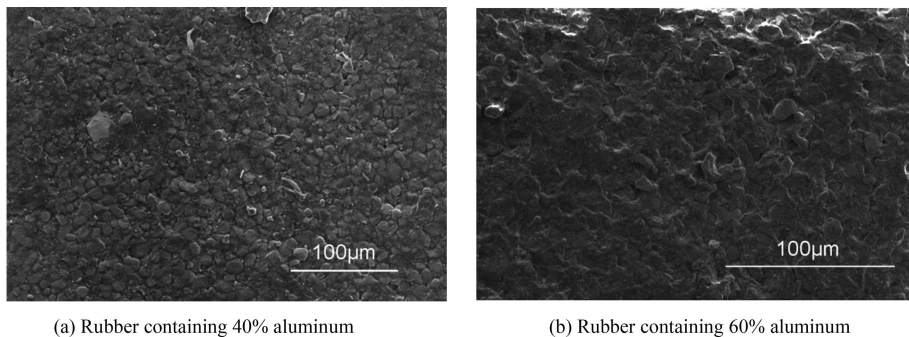


Figure 8. SEM micrographs of rubber containing different proportions of aluminum.

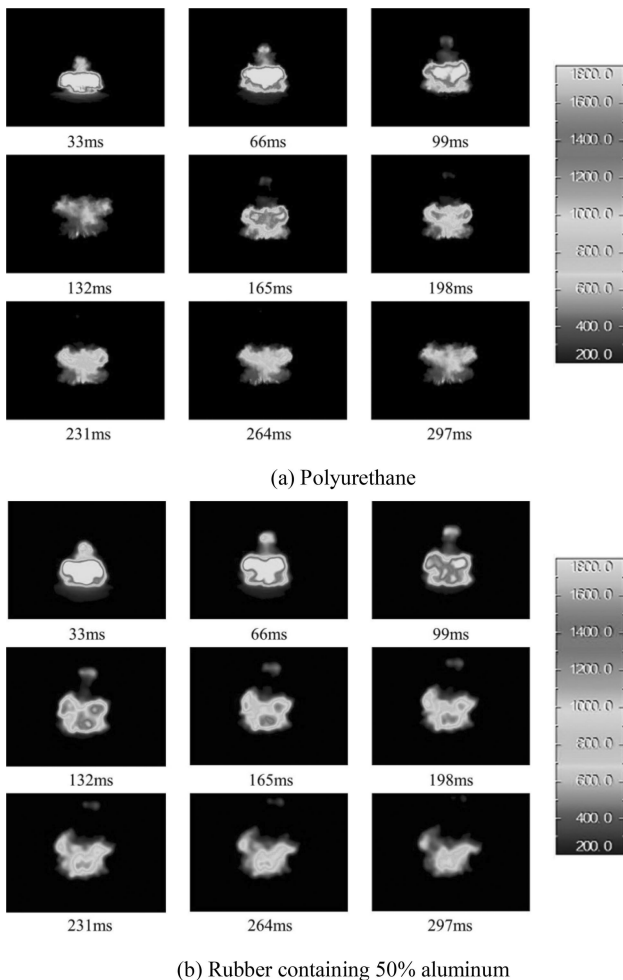


Figure 9. Temperature distribution of fireball surface at various stages after explosion of composite charge at different times for non-detonative materials of a) polyurethane and b) rubber containing 50% aluminum.

of the viscoelastic polymer provided resistance to external deformation of the tensile stress. The non-linear fracture of this polymer molecular chain was caused by the rupture of the non-detonative materials and lateral dispersal.

To further compare the effect of the inert and active non-detonative materials on the explosive fireball temperature, the emissivity was adjusted to 1, and the relative maximum temperature was used. At the highest temperature, the fireball surface was painted with four lines, with two horizontal lines crossing two vertical lines. The temperature distributions along these lines were analyzed. Comparison of Figure 10a and Figure 10b reveals that the non-detonative fireballs of the active non-detonative materials were larger in diameter and smaller in height. The maximum temperature of the active non-detonative body was greater than that of the inert non-detonative body. The temperature of the surface of the inert non-detonative material fireball appeared as a single peak in the horizontal direction, whereas that of the active non-detonative material appeared as a double peak. These results indicate that after being detonated by the central charge, the active non-detonative material cracked and reacted first, and this energy was coupled with that of the outer aluminum-containing explosive. In the longitudinal direction, the center-left C-line passed directly from the edge through the higher temperature region and thus formed a single peak, whereas the D-line in the center position passed from the outer edge first through the high-pressure cloud and jetted upward from the center position and then through the center. In the high-temperature region, the high-pressure region reflected by the ground finally passed through the low-temperature region, thus forming three peaks. For the rubber containing 50% aluminum, the maximum temperature in the transverse direction increased by 23.08% compared with that for polyurethane, and the maximum temperature in the longitudinal direction increased by approximately 16.67%. These results indicate that in the central detonation mode, the use of an active non-detonative body as a non-detonative material can effectively improve the damage efficiency in the killing area.

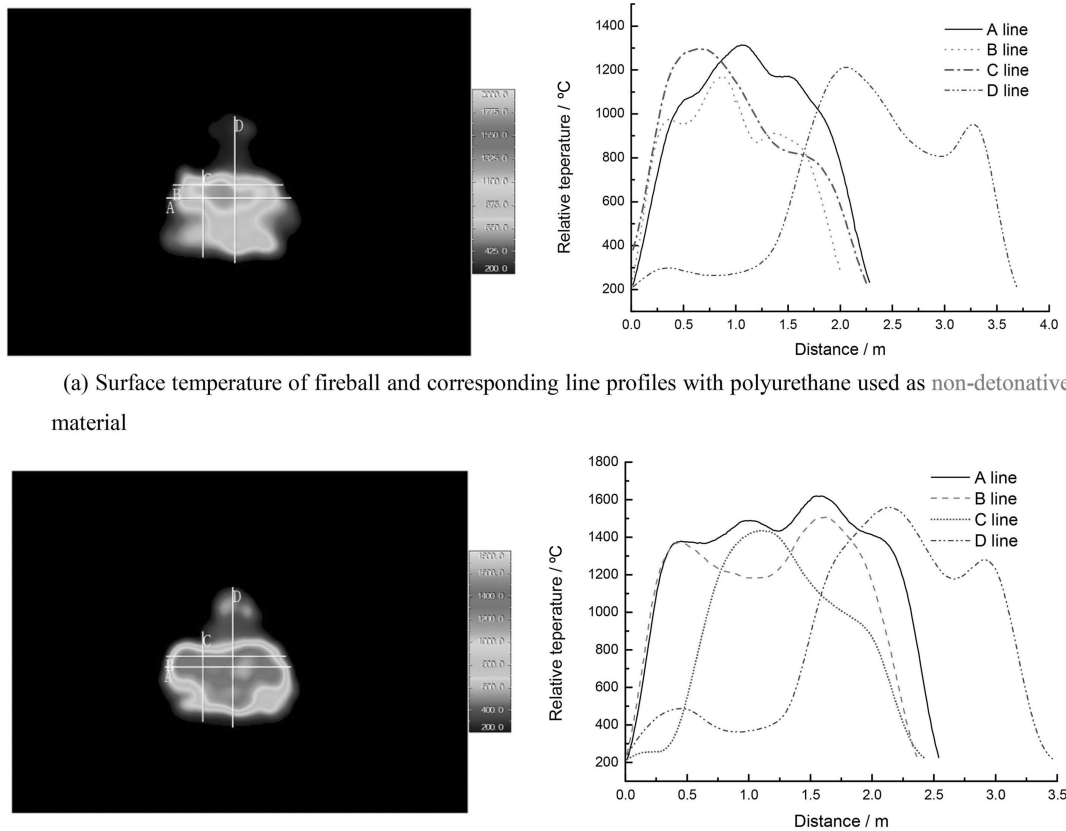
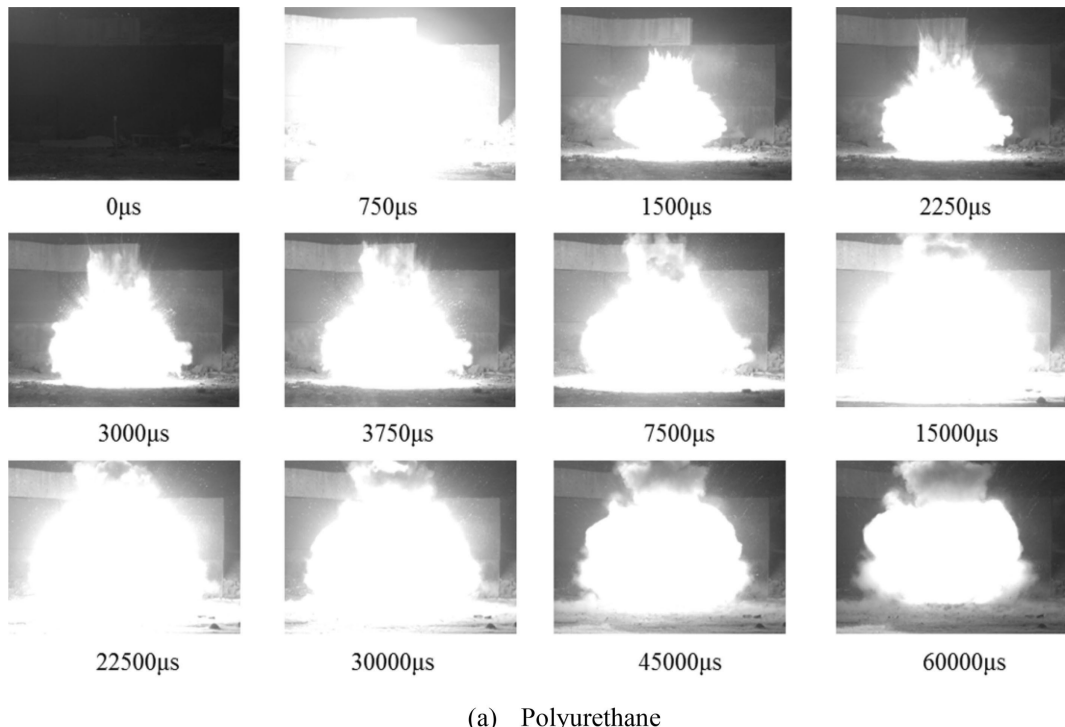


Figure 10. Maximum temperature of explosive fireball and corresponding temperature line profiles for emissivity of 1.

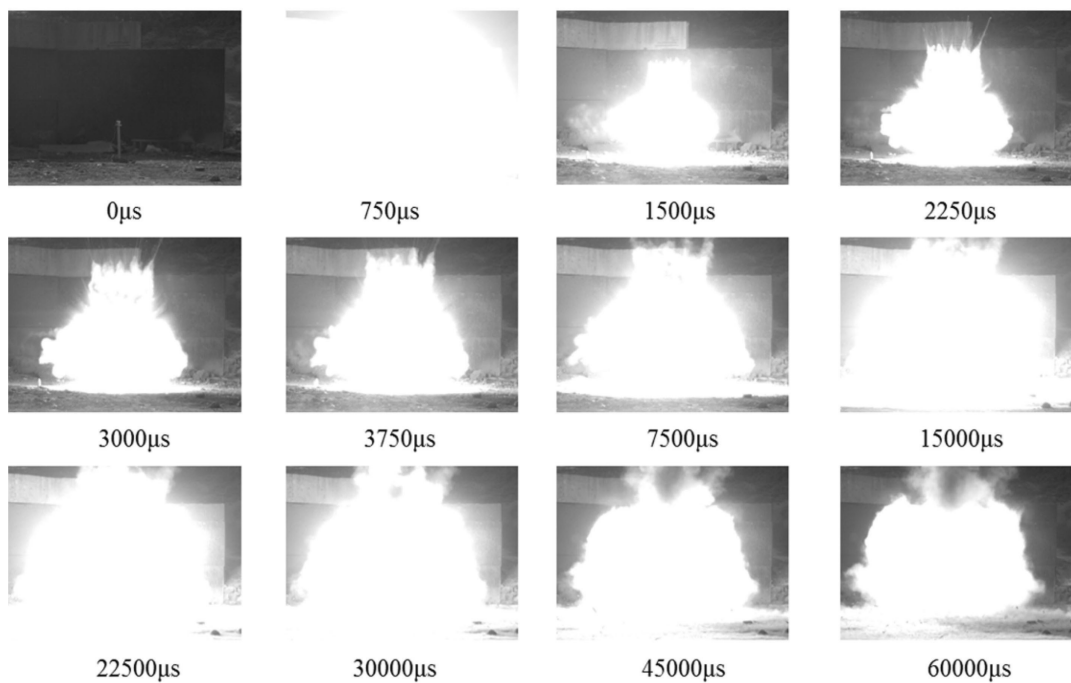
3.2 Analysis of Growth and Reaction Process of Explosive Fireball with Composite Charges

High-velocity photographs were recorded for comparative analysis of polyurethane and rubber containing 50% aluminum as non-detonative materials for explosion of the product and fireball ball expansion process, as shown in Figure 11. Based on the characteristics of the reaction of the thermobaric charges, the explosion process of the composite charge explosive fireball was analyzed. The energy release reaction of the composite charge can be roughly divided into three processes: (1) The initial oxygen-free explosion reaction, mainly of the middle JH-2 explosive molecular compound. This reaction did not require the participation of oxygen in the air, and the duration was as short as less than 1 μ s. (2) The anaerobic combustion reaction after the central charge explosion; for the active non-detonative materials, CO_2 , CO , and H_2O in the first stage explosion products were at high temperature. The aluminum powder in the active material first reacted under high pressure and then reacted again with the aluminum powder in the outer aluminum-containing explosive. The reaction at this stage was also free of external air, and the duration was

less than 1000 μ s. The non-detonative material directly reacted with the aluminum powder in the outer explosive. The difference between the two is clear from the sizes of the fireballs at 750 μ s in Figure 11a and 11b. (3) Explosion after the aerobic combustion reaction, which was mainly the rapid combustion reaction of the rubber and aluminum powder in the active non-detonative material after the central charge explosion; C , H , and CO in the explosion products; and oxygen in the air. The duration was a few tens of milliseconds. The first two processes of the inert and active non-detonative material ended at approximately 1500 μ s (third frame of Figure 11); in addition, the combustion of the composite charges with the inert and active non-detonative materials lasted a certain amount of time. For the combustion effect, the post-combustion time of the active non-detonative material was longer than that of the inert non-detonative material. The post-combustion of the inert non-detonative material was mostly completed after approximately 30 ms (Figure 11a, frame 10), whereas that of the active non-detonative material was not yet finished after 60 ms.



(a) Polyurethane



(b) Rubber containing 50% aluminum

Figure 11. Dispersion process of explosive product of (a) inert non-detonative material (polyurethane) and (b) active non-detonative material (rubber containing 50 % aluminum).

Table 3. Explosion cloud expansion radius fitting coefficients for different non-detonative materials.

non-detonative material	$R(t) = K[1 - B \exp(-Ct^2)]$				The precision of one fitting [%]	Quadratic fitting [%]
	K_1	K_2	B	C		
Polyurethane	2.87	2.86	0.41	0.05	94.99	95.90
30%Al/Rubber	3.03	3.04	0.44	0.06	96.44	96.76
40%Al/Rubber	3.13	3.15	0.43	0.06	96.70	96.90
50%Al/Rubber	3.07	3.04	0.43	0.05	97.95	97.90
60%Al/Rubber	2.92	2.93	0.40	0.05	91.77	93.34

3.3 Distribution of Explosive Products of Composite Charge

AUTOCAD software was used to process the high-velocity photographic data of the explosive cloud expansion process, read the 2D plane image of the explosive fireball, and record the expansion radius of the explosive fireball. An exponential function was used to fit the data of the radius R and time t , and the following relation was deduced between the expansion radius and time for the explosion product of the post-combustion stage:

$$R(t) = K[1 - B \exp(-Ct^2)] \quad (5)$$

where K , B , and C are constants; T is the explosive product dispersal time (ms); and R is the corresponding dispersal radius (m). According to the property of an exponential function as $t \rightarrow \infty$, the final dispersal radius is K . Table 3 presents the fitting coefficients of the expansion radius of the explosive products of the different non-detonative materials and gives the fitting precision. The accuracy of the first fitting was determined using an exponential relation algorithm based on the test data, and the precision of the second fitting was determined using the exponential fitting method with fixed B and C after the K , B , and C were averaged.

The second-order fitting of the data in Table 3 was used to characterize the effect of different non-detonative materials on the change of the expansive radius of the cloud of explosive products. The final values of B and C were 0.41 and 0.05, respectively. The value of K differed depending on the nature of the non-detonative material.

The relationship between the expansion velocity and time of the explosion clouds was determined from the differential equation of the expansion radius:

$$V(t) = 2KBCt \exp(-Ct^2) \quad (6)$$

The relationships between the expansion radius, dispersal velocity, and time for the explosive products for the different non-detonative materials were determined using the fitting coefficients for the second fitting:

$$V(t) = 0.041Kt \exp(-0.05t^2) \quad (7)$$

The relationship between the experimental data, fitting curve, expansion radius of the fireball, dispersal velocity, and time t of the fireball in the post-combustion stage are shown for the non-detonative material of rubber containing 50% aluminum in Figure 12 and Figure 13. Figure 12 shows that the trend of the dispersal radius described by the fitting function with time is consistent with the test data, and the fitting accuracy is 97.90%. Figure 13 shows the relationship between the fireball expansion radius R , scattering velocity v , and time t in the post-combustion phase. In the post-combustion phase, the expansion radius of the explosive fireball increased more rapidly and then slowly changed and tended to stabilize within 3–9 ms. The fireball velocity began to stabilize and then showed a decreasing trend; this behavior is indistinguishable from that of the scattering process of a single thermobaric charge [9]. The dispersal velocity of a single thermobaric charge gradually decreases, and the expansion radius slowly increases. The reason for this behavior is that the non-detonative material with the composite charge structure hindered the expansion of the fireball.

The other non-detonative materials showed similar regularity in the expansion radius and dispersal velocity of the fireball, as observed in Figure 14.

Combining Eq. (7) and Figure 14, it can be concluded that the dispersal velocity of the active non-detonative ma-

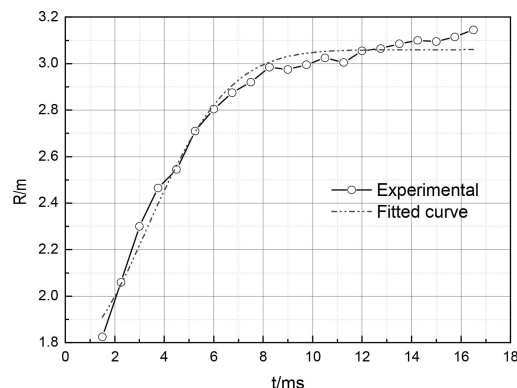


Figure 12. Dispersal radius as a function of time for 50% Al/rubber.

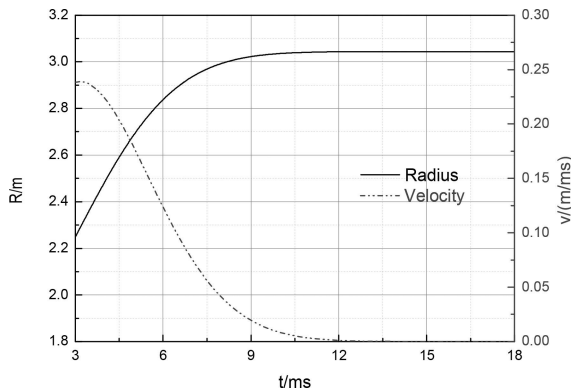


Figure 13. Expansion radius and dispersal velocity as a function of time for 50%Al/rubber.

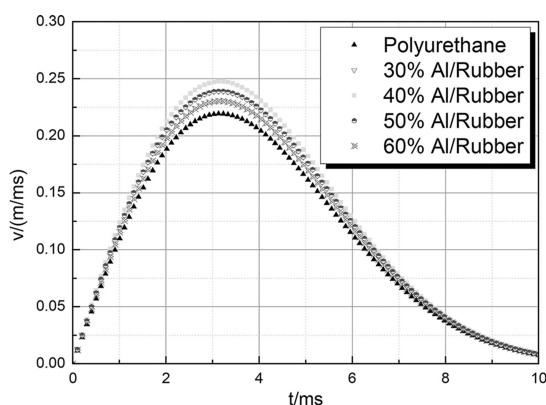


Figure 14. Variation curves of fireball dispersal velocity as a function of time.

material was higher than that of the inert non-detonative material and that the value of the K characterizing the performance of the non-detonative material was large. Because the inert non-detonative material did not contain aluminum powder, aluminum powder was not involved in the reaction of the detonation material after detonation of the center charge. In contrast, because the aluminum-containing rubber contained aluminum powder, the reaction of aluminum powder with the detonation products of the center charge and the oxygen in the surrounding air generated Al_2O_3 , thereby releasing heat energy. This heat energy enhanced the impulse to the external aluminum-containing explosives, resulting in a higher spraying velocity. In addition, with increasing aluminum powder content in the aluminum-containing rubber, the explosion velocity of the explosion product cloud group first increased and then decreased. This behavior was observed because although the amount of heat released by the aluminum powder and impulse increased, the aluminum powder content also increased. After further increase of the aluminum content, because of the high explosion temperature of the central charge, the amount of Al_2O generated from the reaction

with the aluminum-containing rubber aluminum powder increased, the endothermic effect of the formation of Al_2O_3 was greater than the exothermic effect [16], and the amount of released heat decreased accordingly. This phenomenon reduced the intensity of the detonation wave front and the throwing effect on the outer aluminum-containing explosives, which in turn reduced the dispersal velocity. Based on the analysis of the shock wave overpressure, infrared heat radiation, and dispersion radius and scattering velocity, selection of 50% aluminum-containing rubber as the non-detonative material would be advantageous in the design of a power-control warhead to increase the energy release rate and reduce the incidental damage radius.

4 Conclusion

(1) Measurements of the explosive overpressure and infrared thermal imaging temperature of composite charges revealed that the inert non-detonative material (polyurethane) and active non-detonative material (rubber containing 50% aluminum) both showed good explosion-proof performance. The fireball temperature distribution of the active non-detonative material was inhomogeneous. In the lateral direction, because of the energy coupling between the aluminum powder and internal charge, two regions with higher temperature were generated. In contrast, the energy coupling between the inert non-detonative material and external charge only produced one high-temperature region.

(2) The explosion of the composite charge in the central detonation mode was similar to that of a thermobaric charge and consisted of three processes: an oxygen-free explosion process, an anaerobic combustion process, and an aerobic combustion process (post-combustion reaction). There were no clear differences between the active non-detonative materials and the inert non-detonative material for the first two processes; however, the duration of the post-combustion process for the active non-detonative materials was much longer than that for the inert non-detonative material.

(3) The time-dependent curve of the dispersion radius of the composite charge in the central detonation mode obeyed the exponential relationship $R(t) = K[1 - B \exp(-Ct^2)]$. In the post-combustion process, the explosive fireball rapidly increased from 3 to 9 ms and then slowly changed and tended to stabilize after 9 ms. During the initial process, the fireball dispersion velocity changed steadily. Consequently, the K value of the active non-detonative material was higher than that of the inert non-detonative material and first increased and then decreased with increasing proportion of aluminum powder.

(4) Comprehensive analysis of the effects of the non-detonative materials on the inner high explosive detonation wave attenuation performance, heat radiation energy out-

put, dispersion radius, and moving velocity suggest that 50% aluminum-containing rubber should be preferentially selected as the intermediate non-detonative material for this application.

Acknowledgments

The work presented in this paper has been funded by the National Natural Science Foundation of China under No. 11202103 and Qing-lan Project of Jiangsu Province.

References

- [1] M. E. Colclough, A novel tunable effects explosive charge, *NDIA IM&EM Symposium*, Las Vegas, NV, USA, May 14–17, 2012.
- [2] M. Vittoria, W. Burgess, Sympathetic detonation testing of a dual explosive warhead concept for large diameter warheads, *Insensitive Munitions Technology Symposium*, Williamsburg, VA, USA, June 6–9, 1994.
- [3] B. Nouguez, Dual formulation warheads: a mature technology, *Insensitive Munitions Technology Symposium*, Williamsburg, VA, USA, June 6–9, 1996.
- [4] M. Graswald, E. Rottenkolber, Experimental and numerical modeling progress on flexible warhead technologies providing scalable damage area footprints, *27th International Symposium on Ballistics*, Freiburg, Germany, April 22–26, 2013.
- [5] M. Reynolds, W. Huntington-Thresher, Development of tunable effects warheads, *Def. Technol.* **2016**, 12, 255–262.
- [6] P. Haskins, Kemsing. Controllable output warhead [P]. US: 9109865 B2, 2015.
- [7] W. A. Trzciński, K. Barcz, J. Paszula, S. Cudziło, Investigation of Blast Performance and Solid Residues for Layered Thermobaric Charges, *Propellants Explos. Pyrotech.* **2014**, 39, 40.
- [8] W. A. Trzciński, K. Barcz, Investigation of Blast Wave Characteristics for layered Thermobaric Charges, *Shock Waves* **2012**, 22, 119.
- [9] J. Paszula, W. A. Trzciński, K. Sprzatczak, Detonation Performance of Aluminum-Ammonium Nitrate Explosives, *Cent. Eur. J. Energ. Mater.* **2008**, 5, 3.
- [10] B. Zheng, L. Chen, Y.-S. Ding, Z.-F. Wang, Dispersal process of explosion production of thermobaric explosive, *Explos. Shock Waves* **2008**, 28, 433.
- [11] X.-L. Li, J.-M. Hui, L.-F. Xie, Application of infrared thermos-imaging technology in temperature measurement of cloud explosion, *Chin. J. Energet. Mater.* **2008**, 16, 3.
- [12] L. Maiz, W. A. Trzciński, J. Paszula, Optical spectroscopy to study confined and semi-closed explosions of homogeneous and composite charges, *Optics Lasers Eng.* **2017**, 88, 111.
- [13] L. Maiz, W. A. Trzciński, J. Paszula, Investigation of Fireball temperatures in confined thermobaric explosions, *Propellants Explos. Pyrotech.* **2016**, 42, 142.
- [14] G. M. Carluomagno, G. Cardone, Infrared thermography for convective heat transfer measurements, *Exp. Fluids* **2010**, 49, 1187.
- [15] Y. Qin, W. Xi, X. Li, Research on infrared thermal imaging systems for field temperature measurement, *International Symposium on Photoelectronic Detection and Imaging 2009. Advances in imaging detectors and applications*, Beijing, China, June 17–19, 2009.
- [16] Y. Sun, J.-M. Hui, X.-M. Cao, *Military mixed explosives*, The Publishing House of Ordnance Industry, Beijing, 1995.

Received: April 29, 2018

Revised: August 7, 2018

Published online: October 10, 2018